SARTORIUS

# Gas-Liquid Flow, Oxygen Mass Transfer, and Mixing Characterization of a Transparent Single-Use Bioreactor Model (Biostat STR® 200)

Karl Scheibenbogen[b], Marc Maly[a], Vincent Bernemann[a], Jürgen Fitschen[a], Marco Leupold[b] and Michael Schlüter[a]
[a]*Institute of Multiphase Flows, Hamburg University of Technology*
[b]*Sartorius Stedim Biotech GmbH*

1. **Introduction**

In recent years, the biopharmaceutical industry has had to become more flexible and increase upstream yields, driving the uptake of process intensification strategies such as perfusion.[1] This requires production equipment to support high cell density cell cultures requesting an oxygen uptake rate of 20 mmol $O_2$ $L^{-1}$ $h^{-1}$ and above.[2] Testing equipment capabilities typically involves characterization approaches such as determining oxygen mass transfer, energy input, and mixing performance. A broad measurement database and an appropriate mass transfer model CFD can be applied to better predict culture impact. However, cell activity sometimes deviates from expectations, and empirical validation of the used model is often lacking. In this research, a transparent version of the Biostat STR® 200, made of acrylic glass, was erected at the Institute of Multiphase Flows at Hamburg University of Technology to gain deeper insights into the two-phase flow pattern. The gas distribution and mixing behavior were investigated using high-resolution pictures and videos. In these assessments, two different stirrer combinations have been investigated for varied aeration rates and stirrer frequencies.

With regards to oxygen mass transfer rate, the acrylic reactor replica behaves similarly to the industrial single-use bioreactor system, with deviations lying within the predefined ranges determined by the Sartorius Biostat STR product characterization approach.[3] The volumetric mass transfer coefficient $k_La$ is also comparable for both reactors. Consequently, it can be assumed that the visual recordings from the transparent model reflect dynamics from industrialized single-use cultivation chambers. Furthermore, high-resolution imaging of the acrylic replica of the Biostat STR® 200 enabled the systematic characterization of the mixing and mass transfer performance, helping us to understand the influence of stirrer speeds and gassing rates in combination with different sparger and impeller types as well as their interaction.

2. **Materials & Methods - System Setup**

Based on the technical drawings of the Biostat STR® bag holder and the 200 L Flexsafe STR® standard design supplied by Sartorius, an acrylic twin was constructed to be as identical to the original system as possible, with emphasis put on the headspace and the bottom element of the reactor. All acrylic parts were welded together with Acryfix 192 (Evonik) and treated at higher temperatures for several hours to temper the material tension-free. Four ports for probe and measurement equipment access are also implemented on one side of the reactor. Core elements of the Flexsafe STR® Bags are represented by the inbuild shaft with two stirrer blades attached (vessel to impeller ratio d/D was 0.38, distance between both impellers was 300 mm) and a sparger combination with a circular arrangement of 20 x 0.8 mm bore size and an inner area with 100 x 0.15 mm holes below (Figure 1).

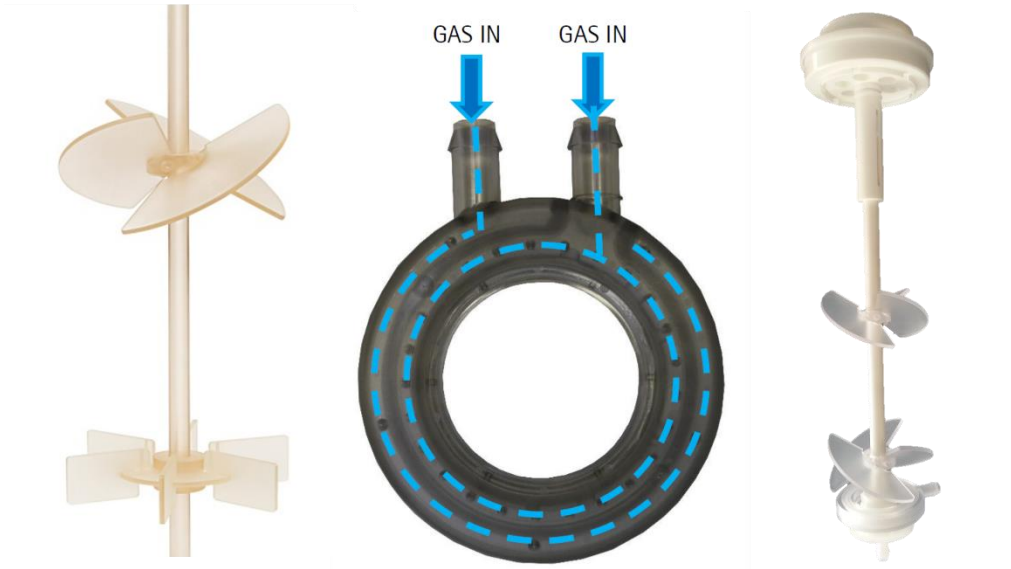


Figure 1 STR shaft with Rushton and Segment impeller, combi sparger, and whole shaft assembly 2x Segment elements (from left to right)

The final assembly was installed in a supporting structure and then fitted with the original shaft, impellers, spargers, and tube sets. Both configurations have been investigated: the Segment-Segment impeller combination, which introduce an axial flow into the system (Figure 3), and the Rushton-Segment assembly, with the Rushton impeller at the bottom part of the shaft (Figure 2). An LED panel was installed behind the reactor to provide homogeneous lighting for optical investigations.

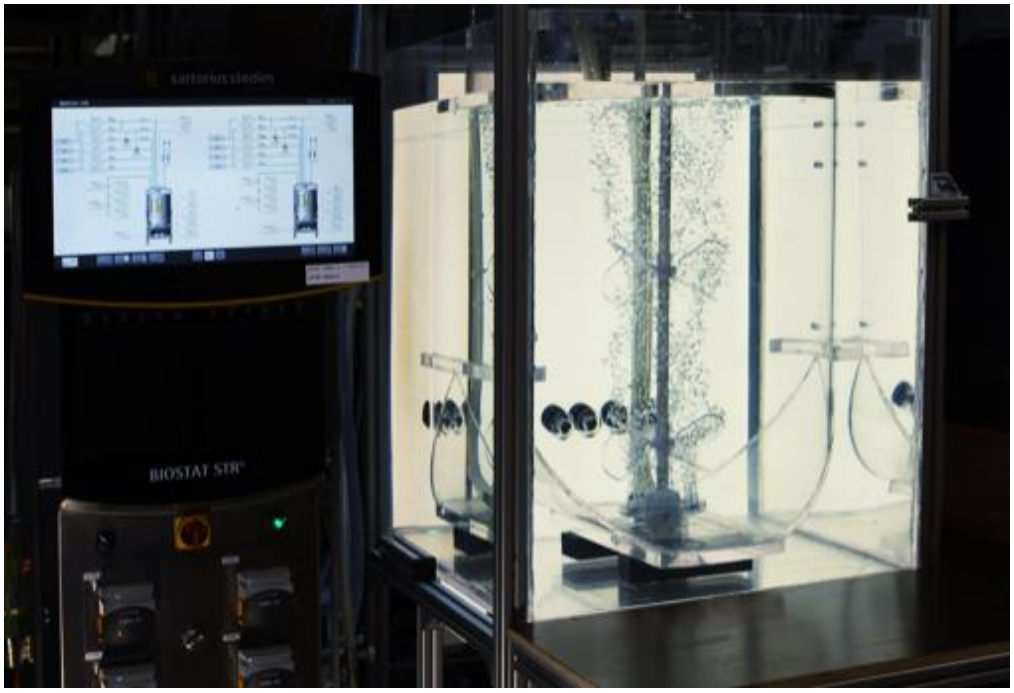


Figure 2 Acrylic twin model STR 200 L connected to Biostat STR® control tower

The acrylic twin model was surrounded by a pool filled with DI water for refractive index matching to avoid distortion of video and camera observations and to temper the reactor volume. High-resolution photos were taken with a commercial camera (*Nikon* D7500) and a

lens (*Carl Zeiss* ZF Planar f 1.4 50 mm) with short exposure times to minimize blur and with a large aperture value *F* to obtain a small field of depth. By pre-calibration with a calibration target within the small field of depth, the relation of pixels per millimeter is known for the exact evaluation of the bubble size distribution. Figure 3 shows a distortion-free image of the reactor.

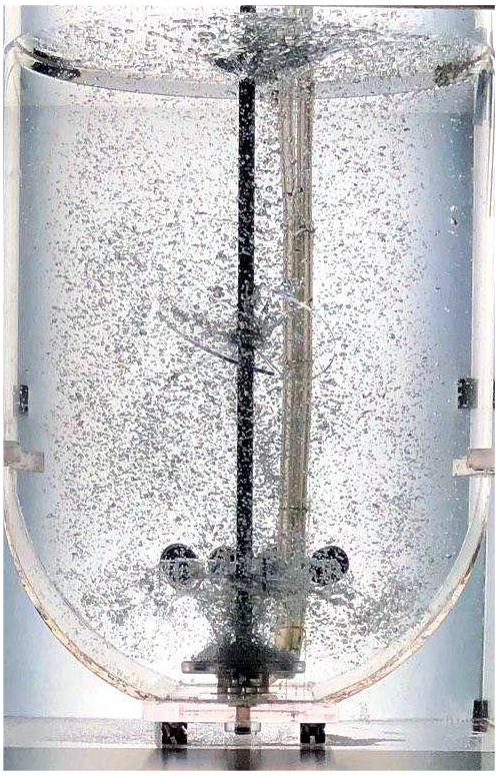

Figure 4 Image of bubble distribution taken with LED backlight method

To obtain reliable bubble size data, we manually evaluated all images, taking into account all bubbles within the focus plane. The video recordings were performed similarly, generating short clips with different parameters related to the whole volume or a specific section of the reactor (see positions in Figure 7) to observe the flow pattern of the bubbles visually.

Further, mixing experiments are conducted by the decolorization of the pH-sensitive tracer Phenolphthalein.[4] The recordings start with the addition of acid from above and continue until the violet color has completely disappeared[8].

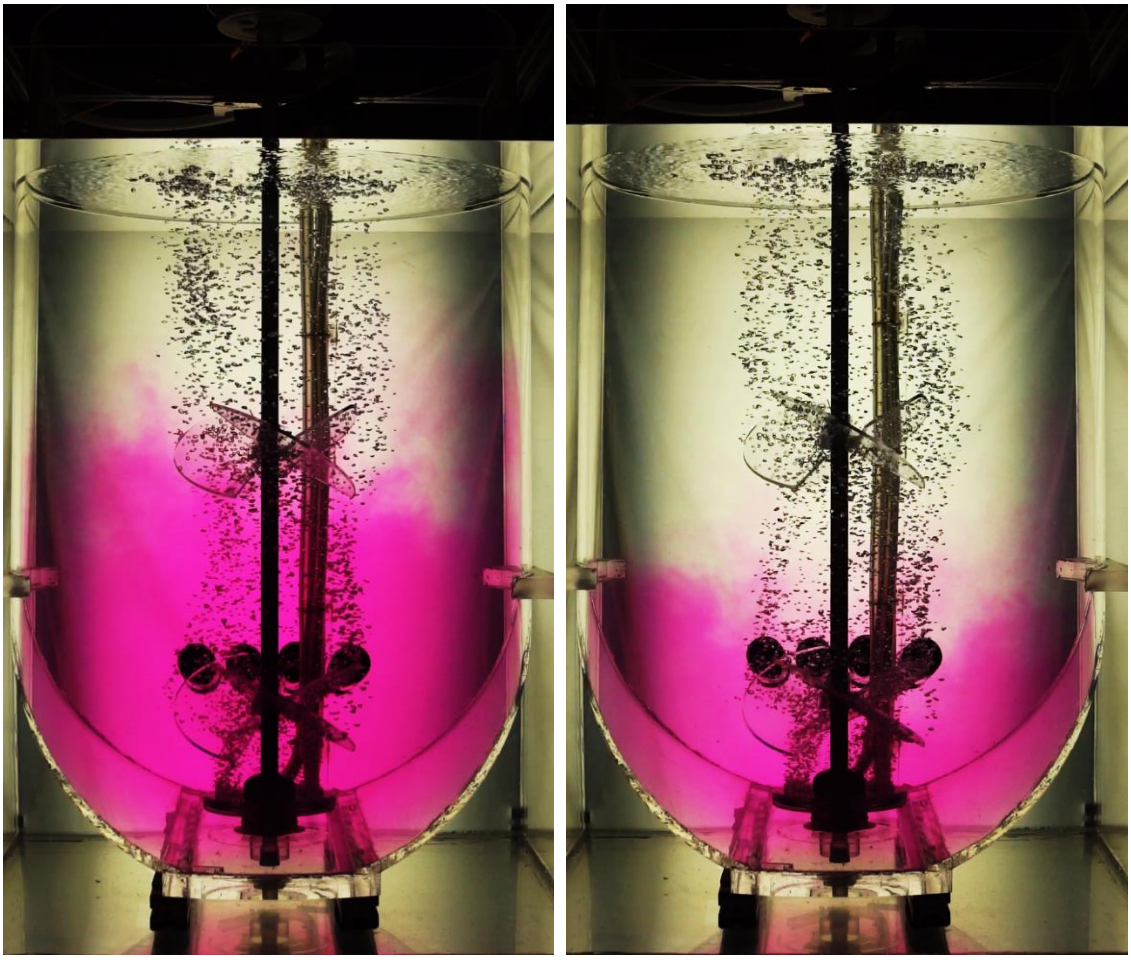

Figure 4 The progress of mixing over time is visualized by the decolorization method. (left) after 18 s and (right) after 41 s of acid addition.

All experimental measurements are conducted for different stirrer frequencies, aeration rates, and both impeller combinations. Figure 4 visualizes decolored volume areas at two different time steps.

Benchmark data on the volumetric mass transfer coefficient $k_La$ in phosphate-buffered saline (PBS) are measured using the dynamic method according to the Dechema Guidelines[5] and compared to data provided by Sartorius Stedim Biotech GmbH. The dissolved oxygen concentration is measured using two optical oxygen probes (WTW FDO©925 and Hamilton Oxyferm XY) at similar positions with respect to the original bag design.

## 3. Characterization

The acrylic glass replica was qualified at the beginning of the measurement campaign by comparing the volumetric mass transfer coefficients of both reactor systems. The aim was to demonstrate similar behavior of the acrylic twin and the original Flexsafe STR® 200 L bag. The final results are shown in Figure 5.

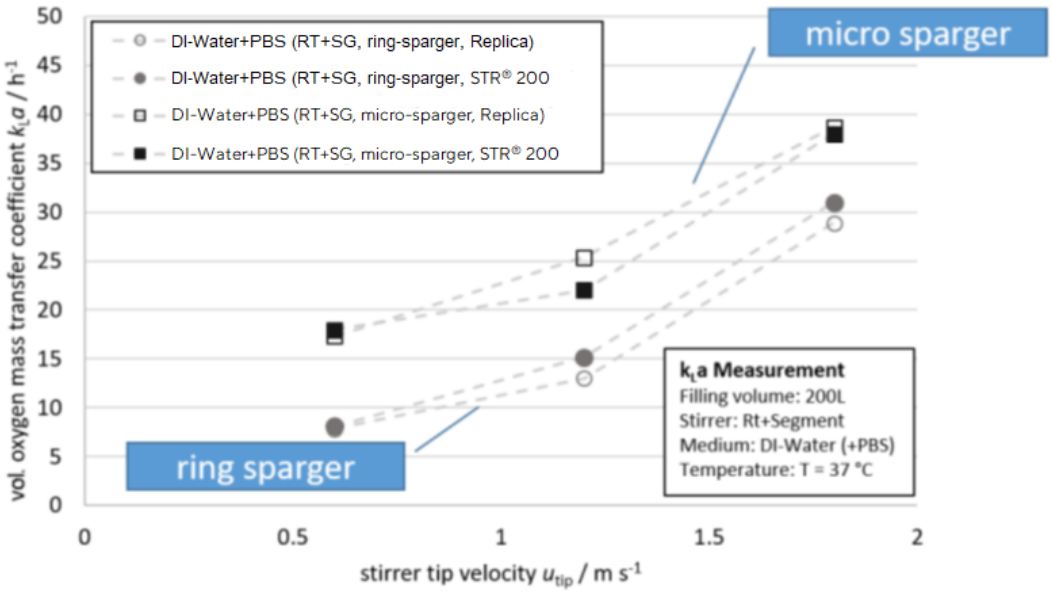


Figure 5 Comparison of the volumetric oxygen mass transfer coefficients between the acrylic replica and the original Biostat STR® 200 with different spargers

The volumetric mass transfer coefficient $k_La$ is comparable for both systems, with minor deviations due to principal measurement uncertainties (e. g., probe response times, local inhomogeneities, sensor calibration). The volumetric mass transfer coefficient $k_La$ links the oxygen transfer rate, which is necessary to maintain aerobic cell cultures, to the minimum dissolved oxygen concentration $c_{O2}$ and the theoretical oxygen saturation $c^*_{O2}$ within the given media:

$$OTR = k_La \cdot (c^*_{O2} - c_{O2}) \qquad \text{Equ. 1}$$

To better understand the influence of different reactor setups, we investigated the dynamics of the gas/liquid flows within the reactor. The flow patterns of the Rushton/Segment or 2x Segment impeller combinations with either the ring- or micro-sparger at various operation conditions were recorded, enabling us to analyze the impact of the impeller and sparger type on the gas/liquid flow dynamics (examples are shown for both sparger variants in Figure 6).

Video clips at varying parameters (stirrer frequencies $n$ = [25, 120, 150] rpm; gassing rates $q$ = [0.5, 6, 13] lpm) show specific bubble rising paths. The respective video sequences are all available online and are linked to at the appropriate sections of the text.

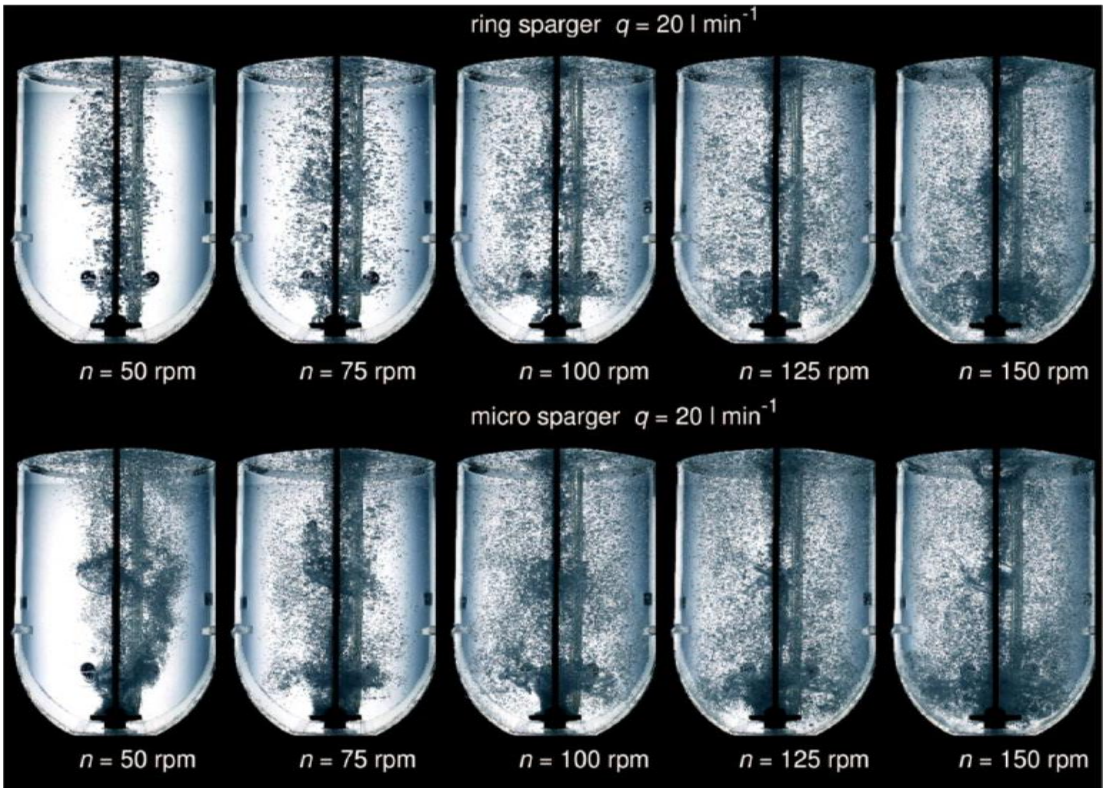


Figure 6 Examples of flow patterns at different stirrer frequencies of a Rushton/Segment stirrer setup at a gassing rate of 0.1 vvm (≙ 20 L min$^{-1}$)

The connection between the volumetric mass transfer coefficient $k_La$ and the gas bubble distribution is the interfacial area $a$, as the total available interface for mass transfer per volume. This interfacial area $a$ depends on the gas hold-up $\varepsilon_G$ as well as the Sauter mean diameter $d_{32}$ according to Eq. 2

$$a = \frac{6\,\varepsilon_G}{d_{32}} \qquad \text{Eq. 2}$$

The Sauter mean diameter $d_{32}$ can be calculated using the bubble size distribution (BSD), which takes into account the bubble volume $V_i$ and the bubble surface area $S_i$. (Eq.3).

$$d_{32} = \frac{6 \cdot \sum_{i=1}^{n} V_i}{\sum_{i=1}^{n} S_i} \qquad \text{Eq. 3}$$

We then compared the BSD and the resulting Sauter mean diameters $d_{32}$ at the highest aeration rate and for three stirrer tip speeds. Figure 7 shows the nine regions of interest (ROI) in which the BSD was evaluated with a high spatial resolution (36 px/mm). The bubbles were assumed to be rotationally symmetric; thus, their volume and surface area can be calculated by an ellipsoidal fitting.

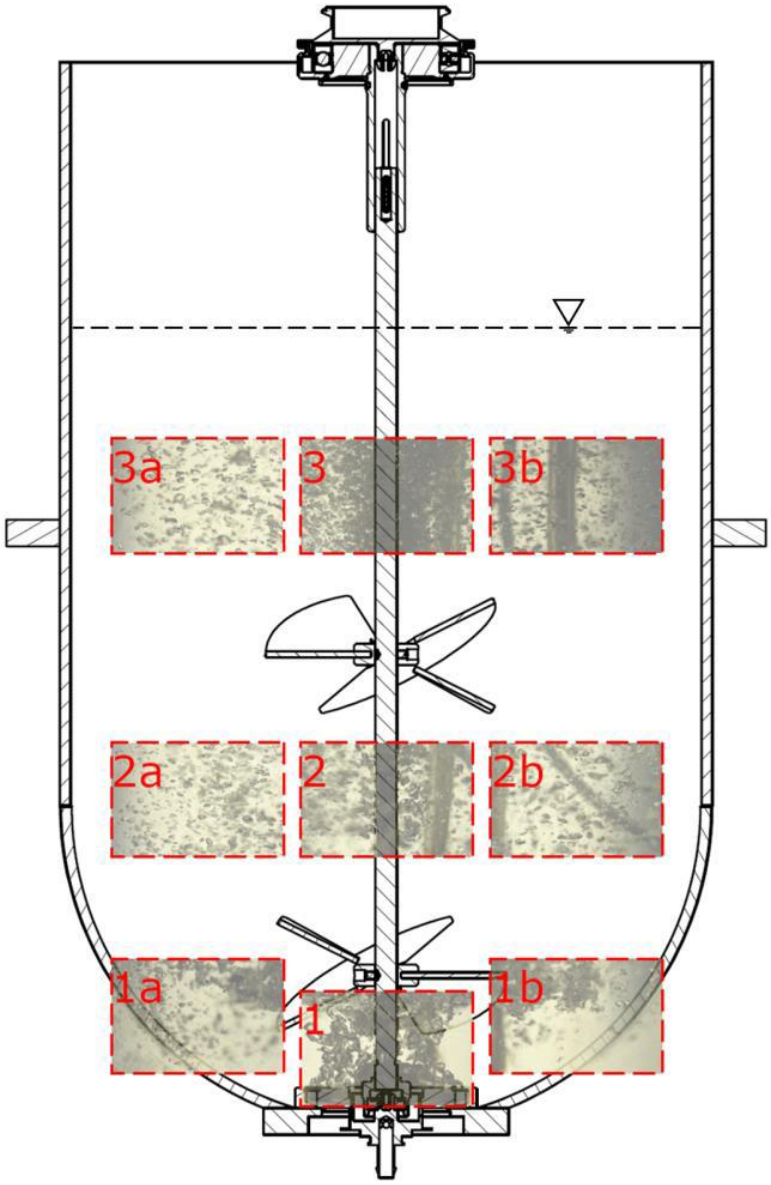


Figure 7 Schematic of the reactor regions of interest for bubble size evaluation

As the investigation of all nine ROIs for all possible combinations of the different parameters (stirrer setups, impeller tip speeds, sparger types, and gassing rates) is very resource intensive, only a selection of parameter combinations was evaluated to offer a good overview. Additionally, the Rushton/Segment impeller results will be shown only for a stirrer frequency n = 100 rpm (1.2 m/s tip speed) equipped with the ring-sparger and an aeration rate of q = 20 L $min^{-1}$.

The resulting Sauter mean diameters $d_{32}$ for all the ROIs are visualized in Figure 8. It can be seen that the initial Sauter mean diameter $d_{32}$ at position 1 (Pos 1), measured directly above the sparger, is well above the average of the other ROIs. Based on the findings, positions 2 (center) and 2a (decentered) were chosen as a good representation of the whole reactor.

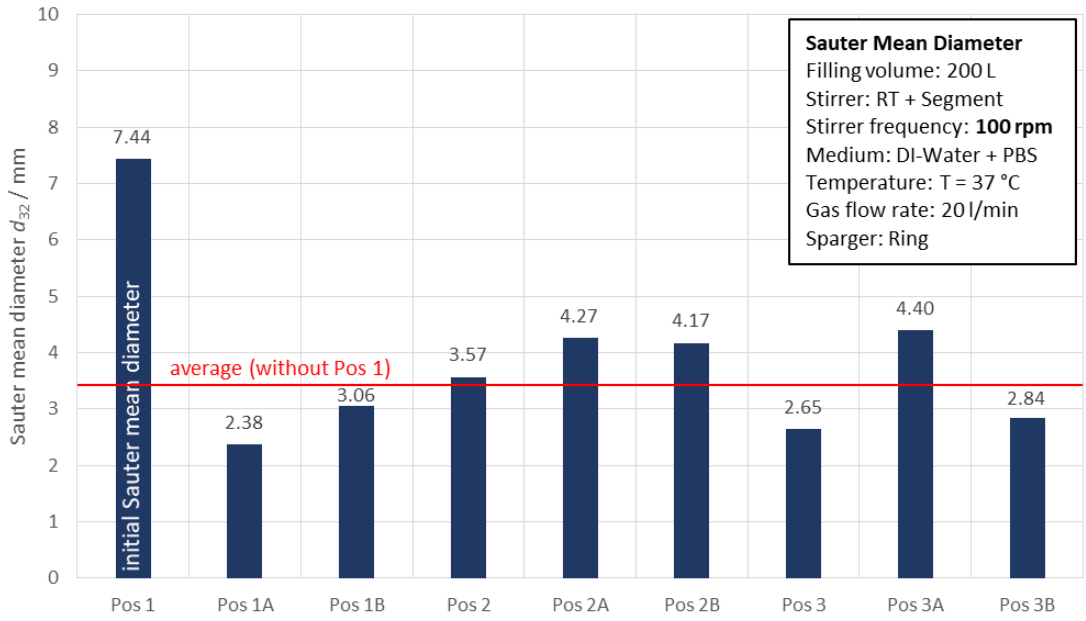


Figure 8 Sauter mean diameters $d_{32}$ for all ROIs investigated

## 4. Results

The following describes the influence of the stirrer configuration and sparger type on the Sauter mean diameters d32. Figure 9 shows the impact of the stirrer frequency on the Sauter mean diameters $d_{32}$ for positions 1, 2, and 3. The initial Sauter mean diameters $d_{32}$ (Pos 1) decreased to about half with increasing tip speed due to the shear forces of the tailing vortices of the Rushton turbine. For the investigated stirrer frequencies n = 50 and 100 rpm, the Sauter mean diameter $d_{32}$ remained nearly constant for positions 2 and 3. At the highest stirrer frequency, the Sauter mean diameter $d_{32}$ at position 3 increased again. In the example recording R_MR_0,5_120_C, the applied low gassing rate of 0.5 L/min shows the dispersion of smaller bubbles into a radial flow pattern, best observed visually.

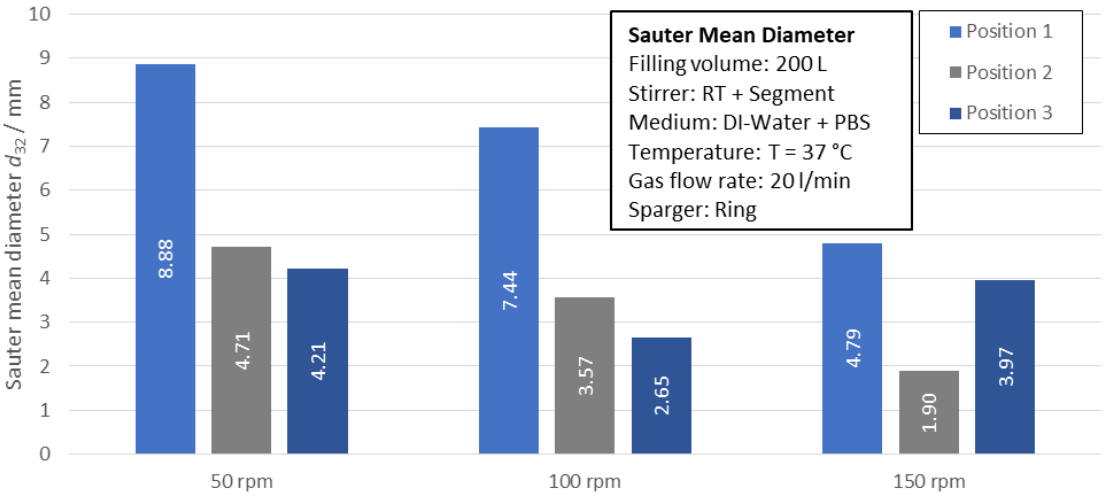


Figure 9 Influence of stirrer speed on $d_{32}$ measured at ROIs along the shaft axes

The observation that the Sauter mean diameter $d_{32}$ remains approximately constant for positions 2 and 3 can be explained by the fact that the upper segment impeller (SG) has a distinctly smaller influence on the bubble dispersion. The effect that the Sauter mean diameter increases again for the highest stirrer frequency at position 3 can be explained by the axial downward directed flow induced by the segment impeller that keeps even the

bigger bubbles, to some extent, underneath the stirrer blades. Consequently, an accumulation of bubbles below the segment stirrer takes place. See recording R_MR_20_150 compared to R_MR_20_120, which shows distinctly higher gas accumulation below the upper impeller at a stirrer frequency $n$ = 150 rpm in contrast to $n$ = 120 rpm. Due to the increased bubble accumulation below the segment impeller, gas particles are also more likely to experience coalescence, and thus the Sauter mean diameter $d_{32}$ increases. In addition, the faster rotating liquid forces the gas phase inwards by a growing centrifugal force.

As a next step, we compared this result to the respective mass transfer coefficient $k_La$ versus the energy dissipation rate calculated as volumetric power input by the Sartorius Process Insight tool.[3] Assuming turbulent flow, the power mainly released by the Rushton turbine leads to a virtually linear increase of $k_La$ values contrasting a similar decrease of the Sauter mean diameter (Figure 10), as expected. For this specific single-use bioreactor, the common behavior of a classical stirred tank is reflected in terms of $O_2$ transfer capability.

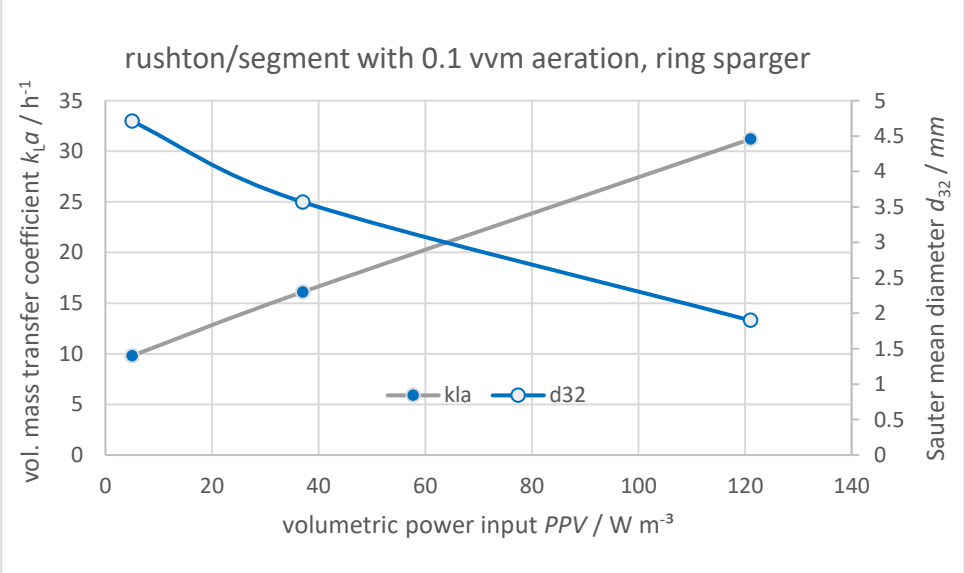


Figure 10 Correlation of oxygen mass transfer coefficient and Sauter mean diameter (measured at pos 2) in dependency of the volumetric power input PPV for a Rushton/Segment Impeller and 200 L filling level

Furthermore, we investigated the differences between the combination of the Rushton/segment stirrer and the double segment stirrer (three blades at 30° angle, downward pumping). The area density distributions and Sauter mean diameter $d_{32}$ at ROI positions 2 and 2a are depicted in Figure 11. The double segment stirrer configuration (Figure 11A) has a much lower influence on $d_{32}$ than the Rushton/segment combination (Figure 11B). This effect can be explained by the much lower power input of a segment stirrer compared to a Ruston turbine at the same stirrer frequencies. At a stirring speed $n$ = 150 rpm, the Sauter mean diameter $d_{32}$ evolving with 2x SG (corresponds to a P/V of 51 W m$^{-3}$) is close to the value of RT+SG at 50 rpm (P/V 5 W m$^{-3}$), demonstrating the impeller impact on energy dissipation.

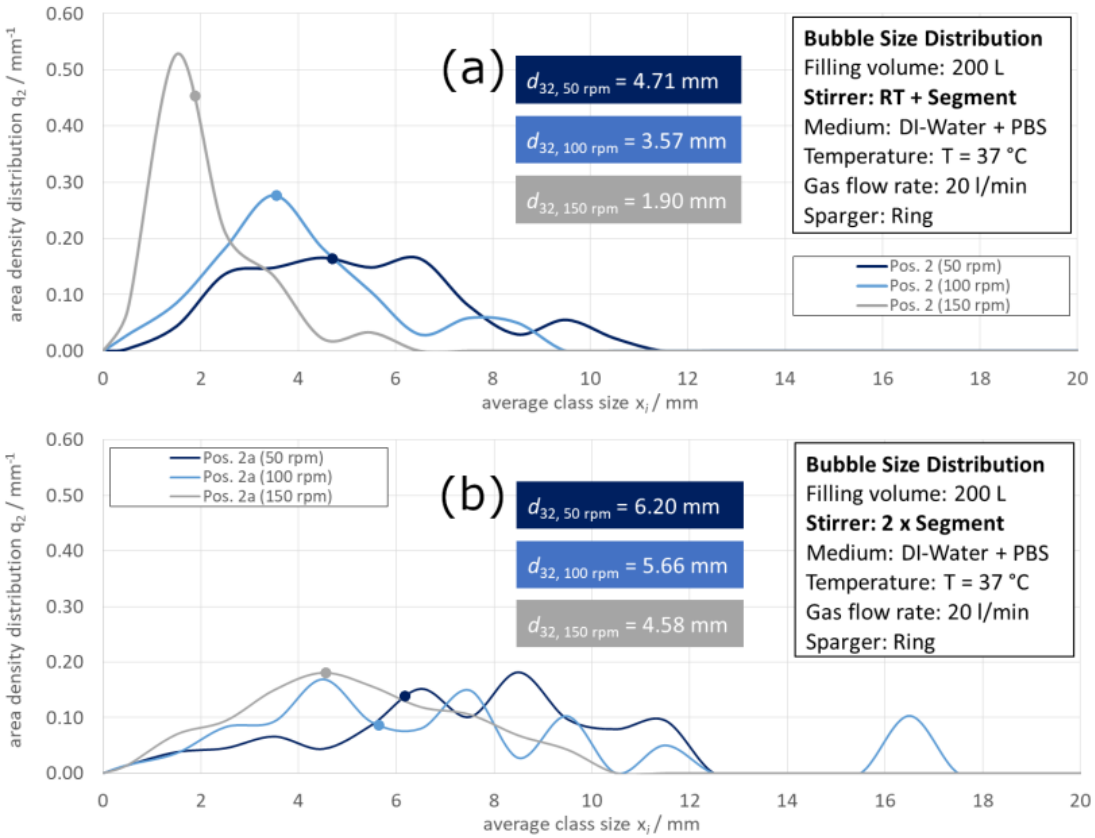


Figure 11 Area density distribution generated with different impeller combinations and stirrer frequencies

Considering $n$ =150 rpm (corresponding to a tip speed of 1.8 m/s), the setup with the Rushton turbine provides the highest energy input (calculated to a PPV of 121 W m$^{-3}$) and highest gassing surface area by small bubble diameters (see $d_{32;\ 150\ rpm}$, Figure 11A), thus reaching maximum $k_La$ values. Figure 11 shows how much the bubbles of a given class size $x_i$ contribute to the total interfacial area. For example, for a stirrer frequency of 150 rpm with the Rushton-segment configuration, 50 % of the surface area consists of bubbles with a diameter of around 1.6 mm. The corresponding Sauter mean diameter $d_{32}$ is illustrated by circles in Figures 11 and 12. Figure 12 incorporates both volumetric oxygen mass transfer coefficient $k_La$, and the Sauter mean diameter $d_{32}$ versus stirrer tip speed $u_{tip}$, which better reflects a scalable parameter.

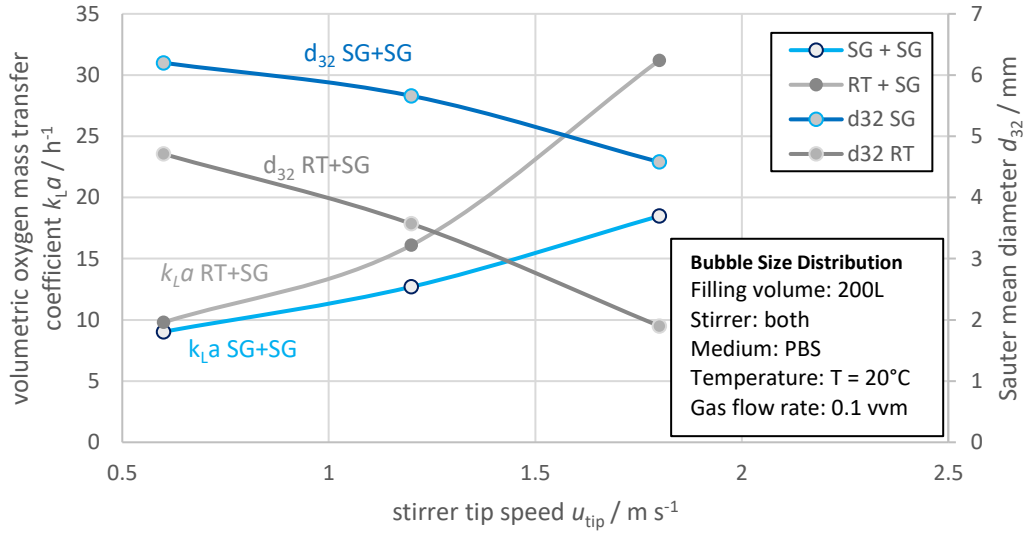


Fig 12 Comparison of $k_La$ and $d_{32}$ at position 2 for the ring sparger versus tip speed

Both mass transfer coefficient and mean bubble size show a distinct contrasting dependency on the stirrer tip speed $u_{tip}$. The recording R_MR_6_120 shows the presence of smaller bubbles compared to R_MM_6_120, clearly visible at lower gassing rates (example given at $n$ = 120 rpm; $q$ = 6 lpm). However, the volumetric oxygen mass transfer performances assimilate at lower stirrer tip speeds for both impeller combinations, though noticeable smaller bubble sizes are generated by the Rushton impeller. At $u_{tip}$ = 0.6 m s$^{-1}$, the $k_La$ values consolidated by Process Insights[3] range between 9 and 10 h$^{-1}$, whereas the measured Sauter mean diameter varies from 4.7 to 6.2 mm. The influence of a Rushton element (with respect to oxygen transfer) only increases significantly towards double SG configuration at higher power inputs PPV, reflected by $u_{tip}$ > 1 m s$^{-1}$. It also seems that bubbles are ascending with similar speed at very low stirrer activity, irrespective of the impeller type (see R_MR_6_25 and R_MM_6_25).

Next, the differences between the micro- and the ring-sparger are determined. Figure 13 shows the area density percentage distributions at position 2a alongside the bubble diameter for the double segment stirrer setup and the use of the micro-sparger for a comparison with the values obtained with the ring-sparger (Figure 11B). Again, it is easy to see that the BSD generated by the micro-sparger is relatively narrow and that the sparger produces very small bubbles with a Sauter mean diameter $d_{32}$ in the range of 2.2 to 2.6 mm. The influence of the Segment stirrers on BSD with increasing stirrer frequency is negligible.

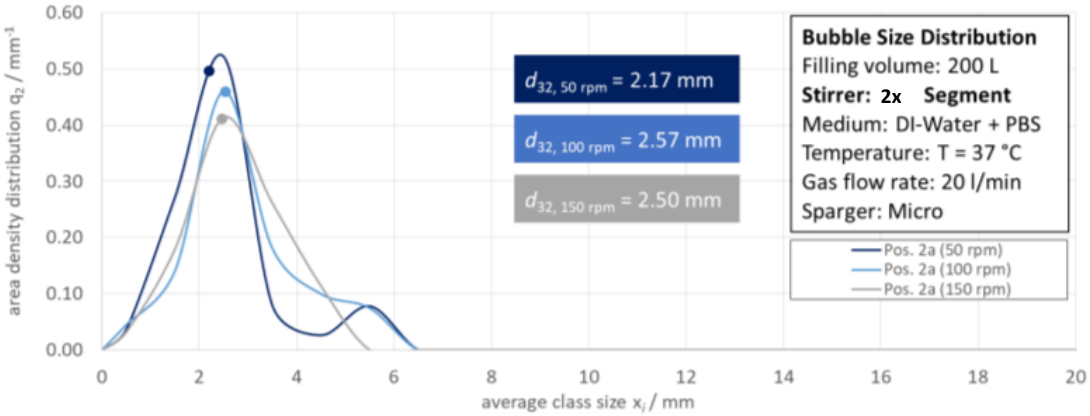


Fig 13 Prevalence of bubbles classified according to their diameter over stirrer speed

However, there is a slight trend towards larger bubbles if higher stirrer frequencies are applied. Small bubbles leaving the sparger ($d_{32}$ = 2.2 mm, see also pos 1, Figure 14) are partially pushed downwards with increasing stirrer speed, and coalescence becomes more likely due to the accumulation of bubbles in the downward flow ($d_{32,\ 100rpm}$ = 2.5). Furthermore, by the associated increased bubble residence time, the almost linear increase of the mass transfer coefficient $k_La$ can be explained (Figure 15), unlikely related to the determined BSD.

The micro-sparger was also investigated within the Rushton/segment stirrer setup. Figure 13 shows the obtained BSD and the Sauter mean diameter $d_{32}$ in the representative regions 2 and 2a, directly above the sparger (position 1), and below the fluid surface (position 3) for the maximum gas flow rate $q$ = 0.1 vvm and a stirrer frequency $n$ = 100 rpm.

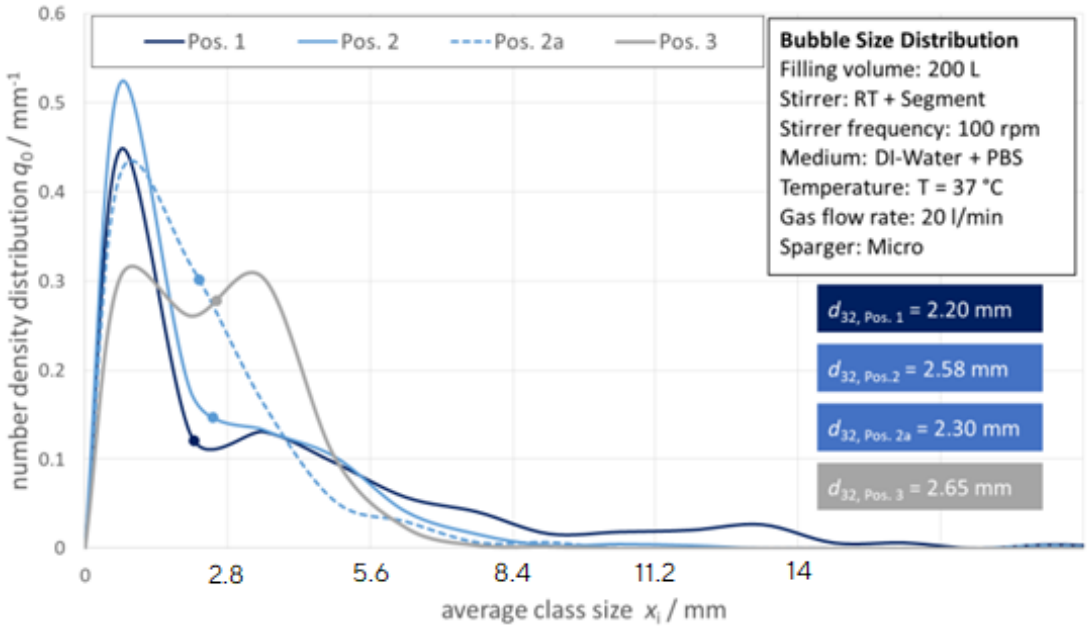

Figure 14 Number density distribution (1=100%) and Sauter mean diameter with RT + SG setup

Figure 14 shows that the initially generated Sauer mean diameter (pos 1) is very small (compared to $d_{32}$ obtained with the ring-sparger in Figure 9). The deviations between the positions are almost negligible with respect to the evaluated $d_{32}$ values. However, the shape of the BSD differs for the selected ROIs. This can be explained again with a slight tendency to gas accumulation below the upper segment impeller, whereas the Rushton element is distributing bubbles in a radial flow (see M_MR_0.5_120). Furthermore, the Rushton turbine has a much smaller effect on the initially generated Sauter mean diameter $d_{32}$ of the micro-sparger, as for the larger bubbles leaving the ring-sparger. However, the Rushton/segment combination with micro-sparger results in the most efficient oxygen transfer, exceeding the performance of the double SG (Figure 15, results SG from Sartorius Process Insight[3] tool) at the highest tip speed $u_{tip}$.

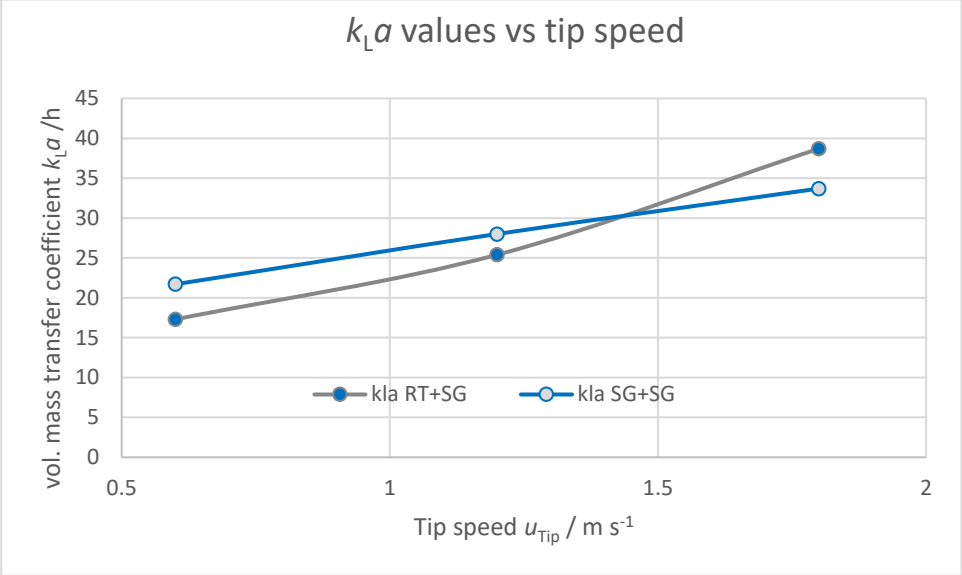


Figure 15 $k_La$ values determined with micro-sparger and both stirrer combinations at max. working volume

The visual analysis of the BSD does not reveal obvious differences between the segment impeller and the Rushton turbine (M_MM_20_150 and M_MR_20_150), even if lower gassing rates and stirrer speeds are applied (see example videos M_MM_6_120 and M_MR_6_120). However, the Rushton turbine appears to achieve a better gas distribution throughout the bioreactor volume. On the other hand, bubbles ascend faster close to the wall area. This may explain smaller $k_La$ values for low and moderate stirrer frequencies, but as for residence time, this could not be quantified with the given experimental configuration. Therefore, no further investigations of this setup within the scope of this work were conducted.

Finally, mixing behavior within non-gassed and gassed combinations was visualized. The significance of the gassing regime on mixing has to be considered.[6]
At high stirrer frequencies, the measured time between the addition of the acid and the complete decolorization was determined with 9 s for the Rushton/segment combination, $n$ = 150 rpm and no gassing (MR_0_0_0_150) and 12 s (2x Segment, n =120 rpm) for gassing with $q$ = 5 lpm (MM_R_5_120) with last color spots in the top area and less impact of stirrer combinations used. Applying a gassing regime with $q$ = 20 lpm and double SG (MM_R_20_120), the violet color is maintained in the bottom area and slightly increased mixing time to 16 s at $n$ = 120 rpm. A transition phase is also observed (MR_R_5_120), showing final violet spots in the top and bottom areas but with less impact on mixing time (13 s).
This change of an inversed flow pattern is even more distinct if lower stirrer speeds $n$ = 25 rpm are considered. The non-gassed example (MM_0_0_0_25) showed residual violet color in the top areas, whereas, with slight aeration $q$ = 3 lpm through the micro-sparger (MM_M_3_25), markers are left close to the sparger region, but both with mixing times > 1 min. However, at a higher gassing rate of $q$ = 10 lpm (ring-sparger; MM_R_10_25), mixing time was lowered by 50% to about 30 s. A similar condition with the Rushton/Segment combination was more effective with respect to mixing MR_0_0_0_25 ($n$ = 25 rpm, no aeration, 36 s). Applied gassing revealed a similar turbulence shift (MR_R_10_25; $n$ = 25 rpm, $q$ = 10 lpm, 33 s) concerning the last spots reached as for the 2x SG configuration (see reactor area reached last in Table 1). However, a low flow aeration regime MR_M_3_25 ($n$ = 25 rpm, $q$ = 3 slpm, 60 s) affected mixing time to almost doubled value compared to non-gassed evaluation. These observed results for mixing times are within the predicted result

window from the Sartorius tool[3](determined by iodometric decolorization method[5]), except for values clearly below 1 minute at *n* = 25 rpm - a stirrer frequency commonly applied for microcarrier cultures only.

| Reactor Set Up Assessed | Reactor Area Reached Last | Mixing Time (Videos) |
|---|---|---|
| RT+SG, no gassing, 150 rpm | ROI pos 3 | 9 s |
| *RT+SG, no gassing, 25 rpm* | ROI pos 3 a & b | *36 s* |
| RT+SG, 3 lpm micro, 25 rpm | ROI pos 1 a & b | 60 s |
| *RT+SG, 10 lpm ring, 25 rpm* | ROI pos 1 a & b | *33 s* |
| RT+SG, 5 lpm ring, 120 rpm | ROI pos 1 a & 3 b | 13 s |
| SG+SG, 5 lpm ring, 120 rpm | ROI pos 3 | 12 s |
| SG+SG, 20 lpm ring, 120 rpm | ROI pos 1 a & b | 16 s |
| SG+SG, no gassing, 25 rpm | ROI pos 3 a & b | 66 s |
| SG+SG, 3 lpm micro, 25 rpm | ROI pos 1 a & b | 69 s |
| *SG+SG, 10 lpm ring, 25 rpm* | ROI pos 1 | *30 s* |

Table 1 Summary of mixing behavior observed from video recordings, unpredicted results in italics

The results listed in Table 1 indicate a shift of poorly mixed areas from top (pos 3) to bottom (pos 1) regions for both stirrer combinations if gassing is applied. However, an impact on mixing time was only observed at low stirrer frequencies. With the RT + SG combination, mixing time could be prolonged; with the SG + SG variant, reduced values become obvious if certain aeration was activated. It seems there is no impact of the sparger type selected; however, the influence of BSD on mixing efficiency was not assessed.

## 5. Discussion

Our results show how the bubble size distribution in an acrylic twin of the Biostat STR® 200, with different combinations of stirrer and gassing elements, affects the flow pattern and the oxygen mass transfer performance.

In the case of the ring-sparger and the Rushton-Segment configuration, the bubble size distribution was shifted to smaller diameters compared to the double segment configuration. The reduction of the Sauter mean diameter was caused by the high energy dissipation at the blade tips of the Rushton turbine, which led to a noticeable improvement in the oxygen mass transfer coefficient $k_La$.

During investigations of the combination of a double segment impeller setup with the ring-sparger, the ability to decrease bubble sizes via shearing and thus increase the specific interface between the phases was less pronounced. This was demonstrated by the maximum achievable $k_La$ value for the investigated setup, measured as 18 $h^{-1,}$ and stands in contrast to the achieved value of 31 $h^{-1}$ determined with a Rushton turbine. The effect of dynamic bubble scattering the different sparger and impeller types is well visualized in the linked high-resolution videos of this work. These videos also demonstrate the need for specific power inputs to distribute bubbles over the reactor volume. If the chosen power input is too low, the gas phase will rise along the shaft axis, and the impellers have no significant impact on the gas phase or the residence time of gas bubbles. Consequently, the oxygen mass transfer capability exhibits similarly poor values at low tip speeds.

The introduction of the micro-sparger achieves a clear improvement of measured mass transfer coefficients. This sparger type initially creates smaller bubbles. Consequently, the stirrer frequency is less important for achievable mass transfer rates. Even at low power inputs by the Segment impeller, the $k_La$ values amount to 15 $h^{-1}$ and show an almost linear increase up to a maximum of 34 $h^{-1}$ in the investigated range. Yet, very similar Sauter mean diameters are observed over the whole range of stirrer frequencies. As also shown in the

videos, the pump-down characteristic of the three-segment blades increasingly ensures that large amounts of bubbles are kept in the system.
At similar energy inputs, smaller $k_La$ values were measured for the Rushton impeller in conjunction with the micro-sparger. These obtained results revealed a noticeably smaller mass transfer performance compared to the double segment stirrer setup. Stirrer frequencies must be drastically increased to achieve $k_La$ values above those obtained with the segment stirrers. The maximum $k_La$ value was measured as 38 $h^{-1}$. This value represented only a minor increase in performance over the double segment stirrer setup at the cost of requiring a doubled power input per volume.

Overall, aeration performance recalculated by the $k_La$ values found (OTR= $k_La \cdot \Delta c_{O2}$), and air gassing could not support the requested oxygen transfer rate with 20 mmol $L^{-1}$ $h^{-1}$. Assuming a required oxygen concentration of 0.07 mmol $L^{-1,}$ a maximum solubility $c^*_{O2}$ of 0.65 mmol $L^{-1}$ corresponding to an $O_2$ enrichment to about 50% of total gas pressure can be estimated to supply sufficient oxygen for high cell density mammalian cultures. The addition of pure $O_2$ via the micro-sparger will lead to very small bubble sizes as they dissolve during their flow path through the bioreactor. The results also suggest that further factors like bubble residence time or impact of energy dissipation on liquid mass transfer coefficient[7] gain more significance. In this case, additives like poloxamer influencing surface tension may be taken into account.

In summary, we note:
- High volumetric power input by Rushton impeller is needed to effectively shear bubbles and generate small Sauter mean diameter from initially large bubble sizes
- The initially small bubbles achieved with a micro-sparger render the use of a Rushton turbine redundant in most cases
- Since the mechanical shear stress negatively affecting cell viability cannot be further increased by higher stirrer tip speed, other measures to improve BSD in the bioreactor like sparger design or flow baffles might be considered
- The shown variations of BSDs obtained and the need to add pure $O_2$ into the bioreactor system may challenge the given characterization models and CFD approaches with respect to oxygen mass transfer and $CO_2$ stripping capability

With reference to the conducted mixing experiments, the obtained results from observations captured on video confirm known data. Mixing times are satisfying at moderate or higher stirrer frequencies. Noteworthy is the fact that applied gassing can initiate a reversal of the flow pattern. At low stirrer activity, the impact of bubbles ascending on mixing time is found to be unexpectedly substantial. Thus, bioreactor process control strategies might have to consider potential gradients built up by more permanent zones of poor mixing. This especially applies to cases where stirrer frequency limitations are imposed due to very shear-sensitive requirements, e. g., microcarrier cultures.

**List of symbols & units used**

| | |
|---|---|
| *BSD* | bubble size distribution |
| $c_{O2}$ | O2 concentration, *max. solubility |
| *CFD* | computed fluid dynamics |
| $d_{32}$ | Sauter mean diameter (mm) |
| $k_La$ | volumetric oxygen mass transfer coefficient ($h^{-1}$) |
| *OTR* | oxygen transfer rate in ($mmol \cdot L^{-1} \cdot h^{-1}$) |
| *PBS* | phosphate buffered saline solution |

| | |
|---|---|
| *PPV* | volumetric stirrer power input ($W \cdot m^{-3}$) |
| *ROI* | region of interest |
| *n* | stirrer rotations per minute rpm |
| *RT* | Rushton turbine impeller |
| *SG* | Segment 3-blade impeller |
| *q* | gassing rate in standard liter per minute (lpm) |
| *vvm* | volume gassing per volume liquid per minute |

**List of videos embedded**

| **BSD** | **description** |
|---|---|
| R_MR_0,5_120_C | Ring-sp, RT+SG, 0.5 lpm, 120 rpm, closeup sparger |
| R_MR_20_150 | Ring-Sp., RT+SG, 20 slpm, 150 rpm, whole volume |
| R_MR_20_120 | Ring-Sp., RT+SG, 20 slpm, 120 rpm, whole volume |
| R_MR_6_120 | Ring-Sparger, RT+SG, 6 slpm, 120 rpm |
| R_MM_6_120 | Ring-Sparger, SG+SG, 6 slpm, 120 rpm |
| R_MR_6_25 | Ring-Sparger, RT+SG, 6 slpm, 25 rpm |
| R_MM_6_25 | Ring-Sparger, SG+SG, 6 slpm, 25 rpm |
| M_MR_0.5_120 | Micro-Sparger, RT + SG, 0.5 slpm, 120 rpm |
| M_MM_20_150 | Micro-Sparger, SG+SG, 20 slpm, 150 rpm |
| M_MR_20_150 | Micro-Sparger, RT+SG, 20 slpm, 150 rpm |
| M_MM_6_120 | Micro-Sparger, SG+SG, 6 slpm, 120 rpm |
| M_MR_6_120 | Micro-Sparger, RT+SG, 6 slpm, 120 rpm |
| **Mixing** | |
| MR_0_0_0_150 | RT+SG, no gassing, 150 rpm |
| MM_R_5_120 | SG+SG, 5 slpm ring, 120 rpm |
| MM_R_20_120 | SG+SG, 20 slpm ring, 120 rpm |
| MM_0_0_0_25 | SG+SG, no gassing, 25 rpm |
| MM_M_3_25 | SG+SG, 3 slpm micro, 25 rpm |
| MM_R_10_25 | SG+SG, 10 slpm ring, 25 rpm |
| MR_0_0_0_25 | RT+SG, no gassing, 25 rpm |
| MR_R_10_25 | RT+SG, 10 slpm ring, 25 rpm |
| MR_M_3_25 | RT+SG, 3 slpm micro, 25 rpm |
| MR_R_5_120 | RT+SG, 5 slpm ring, 120 rpm |

**References**

[1]Croughan MS, Konstantinov KB, Cooney C. The future of industrial bioprocessing: batch or continuous? Biotechnol Bioeng. 2015; 112(4): 648- 651. https://doi.org/10.1002/bit.25529

[2]N. Osterhuis & S. Junne . Design, Applications, and Development of Single-Use Bioreactors: Design, Operation and Novel Applications, in *Bioreactors* https://doi.org/10.1002/9783527683369.ch9, 2016

[3]Sartorius Stedim Biotech GmbH, Process Insights software scaling tool vers.1, based on a wide data set $k_La$ measurements according DECHEMA[5] recommendation

[4]J. Fitschen, M. Maly, A. Rosseburg, J. Wutz, T. Wucherpfennig, M. Schlüter. Influence of Spacing of Multiple Impellers on Power Input in an Industrial-Scale Aerated Stirred Tank Reactor. Chemie Ingenieur Technik, 2019 https://doi.org/10.1002/cite.201900121

[5]http://www.dechema.de/dechema_media/Recommendations for process engineering characterization of single-use bioreactors and mixing systems by using experimental methods (2nd Edition)_2020-ISBN: 978-3-89746-227-4.pdf

[6]K.M. Gezork, W. Bujalski, M. Cooke, A.W. Nienow. The transition from Homogeneous to Heterogeneous Flow in a Gassed, Stirred Vessel. Chem. Engineering Research and Design, Vol 78, 2000, 363-370

[7]V. Linek, M. Kordac, T. Moucha. Mechanism of mass transfer from bubbles in dispersions Part II, Chem. Engineering and Processing, Vol. 44, 2003, 121-130

[8]A. Rosseburg, J. Fitschen, J. Wutz, T. Wucherpfennig, M. Schlüter. Hydrodynamic inhomogeneities in large scale stirred tanks – Influence on mixing time. Chemical Engineering Science, Vol. 188, 2018, 208-220,